Journal of Quantitative Spectroscopy & Radiative Transfer 109 (2008) 2779–2793

Contents lists available at ScienceDirect

Journal of Quantitative Spectroscopy & Radiative Transfer

journal homepage: www.elsevier.com/locate/jqsrt

A *k*-distribution-based radiation code and its computational optimization for an atmospheric general circulation model

Miho Sekiguchi [a,*], Teruyuki Nakajima [b]

[a] *Tokyo University of Marine Science and Technology, Tokyo 135-8533, Japan*
[b] *Center for Climate System Research, University of Tokyo, Chiba 277-8568, Japan*

ARTICLE INFO

Article history:
Received 21 January 2008
Received in revised form
24 July 2008
Accepted 24 July 2008

Keywords:
Radiative transfer
Atmospheric absorption
Radiative forcing
Broadband model

ABSTRACT

The gas absorption process scheme in the broadband radiative transfer code "*mstrn8*", which is used to calculate atmospheric radiative transfer efficiently in a general circulation model, is improved. Three major improvements are made. The first is an update of the database of line absorption parameters and the continuum absorption model. The second is a change to the definition of the selection rule for gas absorption used to choose which absorption bands to include. The last is an upgrade of the optimization method used to decrease the number of quadrature points used for numerical integration in the correlated *k*-distribution approach, thereby realizing higher computational efficiency without losing accuracy. The new radiation package termed "*mstrnX*" computes radiation fluxes and heating rates with errors less than 0.6 W/m^2 and 0.3 K/day, respectively, through the troposphere and the lower stratosphere for any standard AFGL atmospheres. A serious cold bias problem of an atmospheric general circulation model using the ancestor code "*mstrn8*" is almost solved by the upgrade to "*mstrnX*".

1. Introduction

The accuracy required for radiative forcing calculations in climate studies has reached about 0.1 W/m^2 [1] due to the advancements in optical modeling, observations of the earth's atmosphere, and computational efficiency. In this situation there is a large demand for an accurate and rapid radiative transfer scheme that would enable more precise and rapid computation. However, broadband fluxes calculated by using existing radiation codes for general circulation models (GCMs) still include a large variance among themselves in order to attain high computational efficiency. The intercomparison of radiation codes used in climate models (ICRCCM) commenced from 1984; phase-1 compared 41 sets of results [2,3]. The range of radiation flux errors from the reference values calculated by the standard line-by-line (LBL) code is about 15–30 W/m^2 in the longwave (LW) region and 10 W/m^2 in the shortwave (SW) region. Under a whole-sky condition, the error range is considerably larger. The radiation transfer model intercomparison project (RTMIP) [4] has evaluated the variance of the results from LBL computations and those of AGCMs, which participated in the IPCC fourth assessment report. The standard deviations of radiative forcing in the doubling of CO_2 concentration are about 1.0 W/m^2 in the LW and up to 2.0 W/m^2 at the surface level in the SW region. To construct a precise radiation scheme, various atmospheric conditions including gas absorption, aerosol particles, and cloud particles also have to be considered.

* Corresponding author. Tel.:/fax: +81 3 5245 7463.
E-mail address: miho@kaiyodai.ac.jp (M. Sekiguchi).

0022-4073/$ - see front matter © 2008 Elsevier Ltd. All rights reserved.
doi:10.1016/j.jqsrt.2008.07.013

More than ten broadband models have been developed by various organizations. A majority of these models use the correlated-k distribution (CKD) method [5] for nonhomogeneous atmosphere [6]. Atmospheric and Environmental Research Inc. (AER) developed the rapid and accurate broadband model (RRTM) [7]. This model is highly accurate due to the efficient schemes for gas absorption calculations optimized by the LBL model for the HITRAN database. The European Center of Middle-Range Weather Forecast (ECMWF) developed a broadband radiation scheme [8] for their GCM, which has been replaced by a rapid version of RRTM (RRTMG) since 2000 [9]. At the same time, a neural network-based radiative transfer scheme has been developed [10] as an alternative to increase the computational efficiency. The National Center for Atmospheric Research (NCAR) developed a radiation scheme [11,12] for their community climate model (CCM3), by which known biases are considerably improved using the RRTMG.

A broadband radiative transfer code "*mstrn8*" [13] has been implemented in mid 1990s in a series of Center for Climate System Research (CCSR)/National Institute of Environmental Study (NIES) AGCM simulations. The *mstrn8* adopts a unique optimization method, different from those of the aforementioned codes, to decrease the number of quadrature points for the numerical integration of the gas absorption in the CKD approach. However, it is known that the *mstrn8* has an error of about 10% in the radiative heating rate calculation around the tropopause thereby causing a serious cooling bias. It is therefore difficult for this model to meet the recent increased demand for accuracy. We need to improve the gas absorption process of the radiation here to solve these difficulties using *mstrn8*.

In this paper, we upgrade *mstrn8* to *mstrnX* with regard to the following three points, namely, use of new optical databases, treatment of more absorption bands, and adoption of several new optimization schemes for obtaining the CKD parameters. Section 2 introduces the descriptions of *mstrn8* and our improvements. Section 3 presents the results of numerical simulations using AGCM and *mstrnX*. This is followed by discussions and conclusions in Section 4.

2. Improvement of *mstrn8*

2.1. Description of mstrn8

The radiation code *mstrn8*, which was developed in 1995 by CCSR, has been used in CCSR/NIES AGCM. In this code, a spectrum from 0.2 to 200 μm is divided into 18 spectral bands with 37 and 55 integration points in its standard and high-resolution version, respectively; these versions can be selected depending on the accuracy required. The CKD method is adopted for efficient approximation of the wavenumber integration, and the numbers of quadrature points are optimized by a nonlinear optimization. The objective function of the optimization is given by the sum of the mean root square of errors of the radiation flux and the heating rate. This code can also be used to treat Rayleigh and Mie scattering and absorption/emission of particulate matters. The radiative transfer solver uses the two-stream approximation, but in a form of the discrete-ordinate method/adding method expandable to any stream number [14].

Fig. 1 shows a profile of heating rate deviation of *mstrn8*-based values from LBL-values. The calculation was preformed off line to mid-latitude summer (MLS) atmosphere for clear sky condition. The surface is treated as a Lambertian reflector. The SW and LW regions are divided at 4 μm. In the SW region, surface albedo is set to 0.1, the solar zenith angle is 60°, and daytime is assumed half a day in this simulation. These assumptions are used in all radiative transfer calculations in this paper when RTMIP cases are not being considered as explained later. The maximum error in the LW region is about −0.8 K/day at tropopause and about 0.4 K/day in the SW region at the middle of the stratosphere. The difference of the error between the standard and high-resolution versions is found to be insignificant, therefore, the result of the high-resolution version is not shown in the figure. The CCSR/NIES AGCM, implemented using the *mstrn8* code for radiative flux calculations, is known to have a cold bias of about 10 K at the tropics and 5 K at the poles in summer in the tropopause as shown in Fig. 2. The maximum cold bias is observed near the altitudes of maximum error in *mstrn8*.

2.2. Absorption databases and gas absorption bands considered

For calculating the atmospheric energy transfer, the radiative energy in a wide spectral range must be considered while taking into account the line and the continuum absorption of molecules. Spectroscopic parameters of line absorption have been compiled into databases such as a series of HITRAN (HI-resolution TRANsmission) databases developed by a long-running project by the Air Force Cambridge Research Laboratories (AFCRL) in the late 1960s in response to the need for detailed knowledge of the infrared properties of the atmosphere. The latest version of the database is HITRAN 2004 [15]. In the update of HITRAN 1992 to 2004, the total number of lines increased from about 710,000 to about 1,890,000 and the number of species of molecules increased from 31 to 39. The line-by-line radiative transfer model (LBLRTM) has been developed by the AER [16,17] for calculating absorption coefficients using HITRAN 2004. In this study, we have introduced the line parameters of HITRAN 2004 to the new radiation code *mstrnX*. For the continuum absorption calculation, we adopt MT_CKD_1 [18] instead of CKD_0 in the LOWTRAN 7, which was used in *mstrn8*. As compared with CKD_0, the band strength, the pressure and temperature dependencies, and the range of absorption are updated in MT_CKD_1. Heating rate profiles, calculated using the LBL model first with HITRAN 2004 in MT_CKD_1 and then HITRAN 92 in CKD_0, show that the maximum difference in the calculation of the continuum absorption is about 0.3 K/day around the troposphere in the LW and 0.1 K/day around the stratosphere in the SW region.

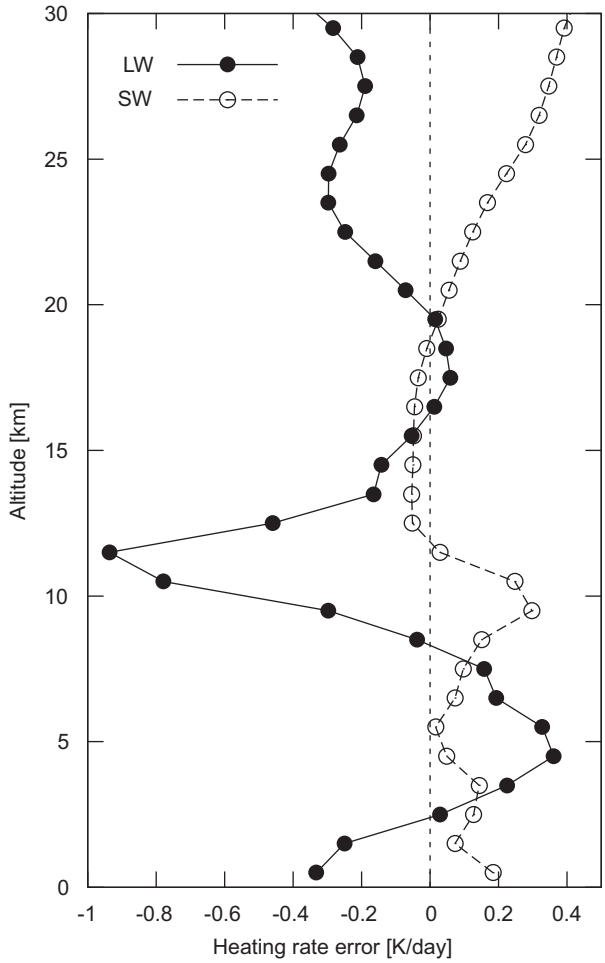

Fig. 1. Error profiles of the heating rate for the mid-latitude summer atmosphere calculated by *mstrn8*. The solid and broken lines indicate results for the LW and SW fluxes, respectively.

In *mstrn8*, H_2O, CO_2, O_3, N_2O, and CH_4 are considered for line absorption bands and H_2O, O_3, and O_2 are considered as continuum absorption bands (Table 1). There are, however, several other important absorption bands which are not listed. When comparing the results of LBL simulation where only those absorption bands in Table 1 are considered to those with the lines of all seven major gases (H_2O, CO_2, O_3, N_2O, CO, CH_4, and O_2), the difference in the radiation flux is about 3.6% and 5.3% in the LW and SW region, respectively. In order to upgrade *mstrn8*, it is necessary to add several other absorption bands for the earth's radiation budget. First of all, we readjust the spectral range of the wavenumber integration. *Mstrn8* defines the SW region from 0.2 to 4 μm and the LW region from 4 to 200 μm; this defines the SW and LW spectral regions. The contribution of terrestrial radiative flux to the SW region is less than approximately 0.86% and the contribution of the extraterrestrial solar irradiance to the LW region is about 0.15%. For simplicity, we neglect this overlap in *mstrnX*, and maintain the same 4-μm boundary between the SW and LW regions. With regard to the lower and upper limits of the spectral region, the contribution from the spectral region of less than 0.2 μm to the solar constant is about 0.03% and the contribution of the terrestrial radiation to the spectral region greater than 200 μm is about 0.005%. These contributions are small and negligible with regard to tropospheric dynamics; however, they are important for chemical reactions and microwave radiative transfer applications. Therefore, the boundary of the LW region is changed to 1000 μm and that of the SW region is changed to 0.185 μm for the GCM applications to in photo-chemical process studies.

Many absorption bands are listed in the HITRAN database; the absorption bands should be selected not according to their band strengths described in the HITRAN database, but according to their influence on the radiative fluxes and also on the heating and cooling rates. The absorption bands and continuum of water vapor are present in spectrum regions greater than 0.4 μm. It has important effects on the atmosphere; therefore, in *mstrnX* we consider water vapor absorption in all spectral bands longer than 0.4 μm. The absorption bands of the other major gases are evaluated as the sum of errors

as shown below

$$f_{\mathrm{obj}} = \sqrt{\sum_{\mathrm{iatm}=1}^{6} (F_{\mathrm{err}}^2 + H_{\mathrm{err}}^2) \Big/ 6} \tag{1}$$

$$F_{\mathrm{err}} = \begin{cases} \dfrac{\sqrt{\int_{\nu_1}^{\nu_2} [F^{\uparrow}_{\mathrm{TOA}} - F^{\uparrow}_{\mathrm{TOA.ref}}]^2 \,\mathrm{d}\nu}}{\int_{\nu_a}^{\nu_b} F^{\uparrow}_{\mathrm{TOA.ref}} \,\mathrm{d}\nu} + \dfrac{\sqrt{\int_{\nu_1}^{\nu_2} [F^{\downarrow}_{\mathrm{sfc}} - F^{\downarrow}_{\mathrm{sfc.ref}}]^2 \,\mathrm{d}\nu}}{\int_{\nu_a}^{\nu_b} F^{\downarrow}_{\mathrm{sfc.ref}} \,\mathrm{d}\nu}, & \text{in LW} \\ \dfrac{\sqrt{\int_{\nu_1}^{\nu_2} [F_{\mathrm{TOA}} - F_{\mathrm{TOA.ref}}]^2 \,\mathrm{d}\nu}}{\int_{\nu_a}^{\nu_b} F_{\mathrm{TOA.ref}} \,\mathrm{d}\nu} + \dfrac{\sqrt{\int_{\nu_1}^{\nu_2} [F_{\mathrm{sfc}} - F_{\mathrm{sfc.ref}}]^2 \,\mathrm{d}\nu}}{\int_{\nu_a}^{\nu_b} F_{\mathrm{sfc.ref}} \,\mathrm{d}\nu}, & \text{in SW} \end{cases}$$

$$H_{\mathrm{err}} = \sqrt{\sum_{l=1}^{\mathrm{NL}} \left(\int_{\nu_1}^{\nu_2} h(l) \,\mathrm{d}\nu - \int_{\nu_1}^{\nu_2} h_{\mathrm{ref}}(l) \,\mathrm{d}\nu \right)^2 \Big/ \sum_{l=1}^{\mathrm{NL}} \int_{\nu_a}^{\nu_b} h_{\mathrm{ref}}^2(l) \,\mathrm{d}\nu}$$

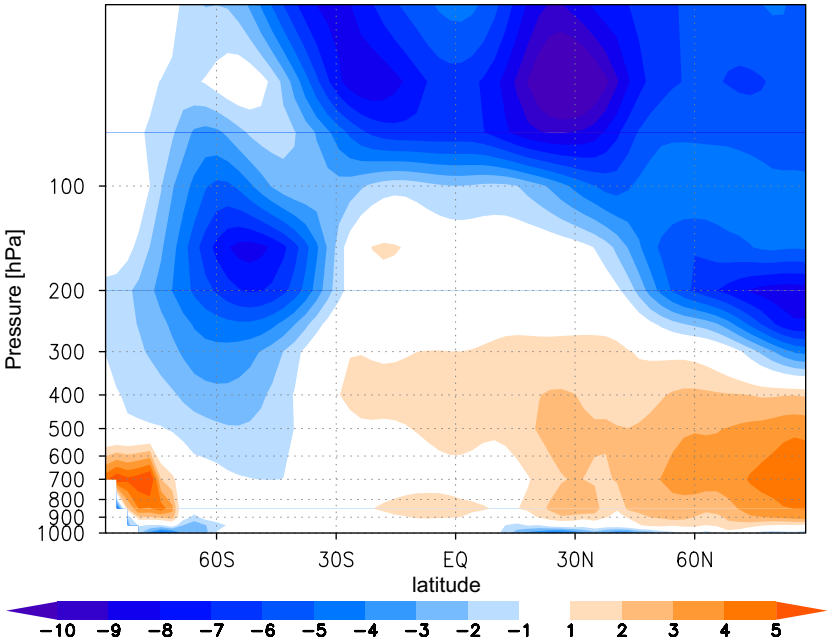

Fig. 2. Latitude–pressure contours of the zonal and three monthly (December, January, and February) mean temperature differences between CCSR/NIES AGCM with *mstrn8* and 15-year means of ERA40 temperature. Units are in K.

Table 1
Wavenumber ranges, implemented gas species, and the number of integration points for the correlated *k*-distribution method in two versions of *mstrn8*

Band limits	Line absorption	Continuum absorption	Low	High
50–250	H_2O		3	5
250–400	H_2O		3	6
400–550	H_2O		3	4
550–770	H_2O, CO_2	H_2O	6	9
770–990	H_2O	H_2O	2	2
990–1100	H_2O, O_3	H_2O	2	4
1100–1400	H_2O, N_2O, CH_4		2	3
1400–2000	H_2O		1	3
2000–2500	H_2O		1	1
2500–4000	H_2O		2	4
4000–14,500	H_2O		5	6
14,500–31,500		H_2O, O_3		
31,500–33,000		O_3		
33,000–34,500		O_3		
34,500–36,000		O_3		
36,000–43,000		O_3, O_2		
43,000–46,000		O_3, O_2		
46,000–50,000		O_3, O_2		

where f_{obj} is the objective function used for band optimization as mentioned later, ν_1 and ν_2 are the spectral band boundaries ($\nu_1 < \nu_2$), ν_a and ν_b are the LW/SW region boundaries ($\nu_a < \nu_b$), $F^{\downarrow}$, $F^{\uparrow}$, and F are downward, upward and net (downward minus upward) radiation fluxes, $h(l)$ is the heating rate with the l-levels calculated in the six AFGL standard atmospheres, and NL is the number of atmospheric layers. The quantities with subscript ref represent the reference values of the radiation flux or heating rate and include all the absorption bands, whereas the quantities without this subscript denote values that do not include a given absorption band in this assessment. Table 2 lists the major gas absorption bands and their effects as calculated by using Eq. (1). The band names and boundaries are referred to those in Liou [19]. The contribution without these listed bands is about 0.131% in the LW and 0.143% in the SW region. We select absorption bands presented in bold type for *mstrnX* with effects greater than 0.1% of the LBL result. It should be noted that this assessment is based on the AFGL standard atmospheres, so it does not ensure the validity for a large change in atmospheric profiles and gas concentrations from those of the standard atmospheres. For example, the N_2O absorption band in 4.5 μm might have quite a large effect in case of the global warming condition. So, we need to prepare the function for each of target atmospheres in a future work.

In case of overlapping band edges (e.g., O_3 in 9.6 μm and N_2O in 7.6 μm), we redefine the band edges to maximize the computational efficiency for calculating the effects of the overlapping bands as listed in Table 3. Furthermore, we divide the spectral region into finer bands in order to take into account the spectral change in the solar spectrum or the Planck function. For example, in the spectral range of 30,000–36,000 cm^{-1}, where only the ozone absorption band exists, two spectral bands are required since solar spectral irradiance decreases rapidly and the strength of ozone absorption increases with a decrease in wavelength.

Concerning water vapor, a foreign-broadening absorption is proportional to the amount of water vapor, whereas a self-broadening absorption is proportional to the square of the water vapor amount. *Mstrn8* considers these two absorption types together by introducing the wavelength-averaged results from LOWTRAN 7. In contrast, *mstrnX* considers these absorption types separately and the foreign-broadening continuum is considered along with the line absorption of the water vapor. This is because both are linearly proportional to the amount of water vapor. Using optical thicknesses

Table 2
Major absorption bands, center wavelengths, band limits, and values of the objective functions (see text)

Gas species	Center wavelength (μm)/ band name	Range (cm^{-1})	$\sum_{iatm=1}^{6} F_{iatm}$	$\sum_{iatm=1}^{6} H_{iatm}$	f_{eval}
CO_2	15 (ν_2)	500–820	8.937	68.06	68.64
	10 (ν_3–ν_1)	820–980	0.105	0.059	0.120
	9	980–1100	0.113	0.102	0.152
	5.0 (ν_1+ν_2)	1900–2200	0.034	0.049	0.060
	4.3 (ν_3)	2200–2400	0.200	1.110	1.128
	2.7 (ν_1+ν_3)	3300–3800	0.001	1.236	1.236
	2.0 ($2\nu_1$)	4700–5200	0.269	0.467	0.539
	1.6 ($3\nu_1$+ν_3)	6000–6400	0.047	0.041	0.063
	1.4 ($3\nu_3$)	6900–7000	0.006	0.050	0.050
O_3	Rotate	10–250	0.000	0.206	0.206
	14 (ν_2)	600–820	0.085	3.181	3.182
	9.6 (ν_1,ν_3)	980–1200	1.965	17.69	17.80
	4.7 (ν_1+ν_3)	2000–2200	0.019	0.112	0.114
	Chappuis	10,000–22,500	1.141	11.63	11.72
	Huggins	30,000–33,000	2.53	8.82	9.17
	Hartley	33,000–50,000	0.186	49.88	49.88
N_2O	17 (ν_2)	550–620	0.108	0.131	0.170
	7.8 (ν_1)	1130–1320	0.387	0.147	0.414
	4.5 (ν_3)	2100–2300	0.066	0.015	0.068
	4.0 ($2\nu_1$)	2500–2600	0.012	0.008	0.015
CH_4	7.6 (ν_4)	1200–1370	0.525	0.460	0.698
	3.3 (ν_3)	2800–3150	0.047	0.105	0.115
	2.3(ν_3+ν_4)	4100–4600	0.087	0.064	0.108
O_2	1.27	7600–8300	0.161	0.103	0.191
	1.0	9100–10,000	0.031	0.016	0.035
	0.76	12,750–13,250	0.371	0.756	0.842
	0.7	14,250–14,750	0.106	0.193	0.220
	vis	15,000–29,870	0.123	0.063	0.138
	Herzberg	36,000–50,000	0.000	0.349	0.349

Table 3
Wavenumber ranges, implemented gas species and the number of *k*-distribution points in three versions of *mstrnX*

Region cm^{-1}	Standard		Global warming		Chemical	
10–250	H_2O, O_3	2	H_2O, O_3	5		5
250–400	H_2O	4	H_2O	8		8
400–530			H_2O	5		5
530–610	H_2O, CO_2, N_2O	2	H_2O, CO_2, N_2O	5		5
610–670		6	H_2O, CO_2, O_3	9		9
670–750	H_2O, CO_2, O_3		H_2O, CO_2, O_3	9		9
750–820			H_2O, CO_2, O_3	2		2
820–980	H_2O, CO_2	1	H_2O, CO_2	2		2
980–1175	H_2O, CO_2, O_3	3	H_2O, CO_2, O_3	5		5
1175–1225		2	H_2O, N_2O, CH_4	2		2
1225–1325	H_2O, N_2O, CH_4		H_2O, N_2O, CH_4	4		4
1325–1400			H_2O, CH_4	2		2
1400–2000	H_2O	1	H_2O	4		4
2000–2500	H_2O, CO_2, O_3	1	H_2O, CO_2, O_3	3		3
2500–3300		4	H_2O, CH_4	2		2
3300–3800			H_2O, CO_2	10		10
3800–4700	H_2O, CO_2, CH_4		H_2O, CH_4	3		3
4700–5200			H_2O, CO_2	5		5
5200–6000			H_2O	4		4
6000–10,000	H_2O, O_2	4	H_2O, O_2	5		5
10,000–12,750		2	H_2O, O_3	3		3
12,750–13,250	H_2O, O_3, O_2		H_2O, O_3, O_2	3		3
13,250–14,750			H_2O, O_3, O_2	2		2
14,750–23,000	H_2O, O_3, O_2	1	H_2O, O_3, O_2	1	14,750–16,667	1
					16,667–20,000	1
					20,000–25,000	1
23,000–30,000		1		1	25,000–28169	1
					28,169–29,412	1
					29,412–30,300	1
30,000–33,500	O_3	2	O_3	2	30,300–31,500	1
					31,500–33,000	1
33,500–36,000	O_3	2	O_3	2	33,000–34,500	2
					34,500–36,000	3
36,000–43,500	O_3, O_2	1	O_3, O_2	2		3
43,500–50,000	O_3, O_2	1	O_3, O_2	1	43,500–46,000	3
					46,000–50,000	3
			O_3, O_2		50,000–54,000	1
Total		40		111		126

calculated by LBLRTM, absorption coefficients are defined as follows:

$$k_{\mathrm{s-cont}} = \tau_{\mathrm{s-cont}}/a^2_{\mathrm{H_2O}}$$
$$k_{\mathrm{line+f\_cont}} = \tau_{\mathrm{line+f\_cont}}/a_{\mathrm{H_2O}} \quad (2)$$

where k is the absorption coefficient, τ is the optical thickness, the subscripts s_cont and line+f_cont mean the self-broadening and the sum of the foreign-broadening continuum and the line absorption of water vapor, respectively, and $a_{\mathrm{H_2O}}$ indicates the amount of water vapor. These absorption coefficients are tabulated and introduced by a look-up table method in the radiative transfer code. We also consider the CO_2 continuum with the line absorption of CO_2; this is not considered in *mstrn8*. The wavenumber ranges of the continuum absorption of ozone and oxygen are broader in MT_CKD_1 than in CKD_0 that is used in *mstrn8*. The continuum absorption is combined with the line absorption for each gas in *mstrnX*.

In *mstrn8*, the correlated *k*-coefficients for the line absorptions in each spectral band are calculated at ten prescribed pressures and five prescribed temperatures, and are fitted to quadratic functions in order to construct look-up tables of the fitting coefficients. The coefficients of the continuum absorption are averaged with the weight of the solar spectrum (or the Planck function for the terrestrial radiation) in each spectral band and are fitted to a quadratic function of temperature to tabulate the fitting coefficients. This tabulated fitting coefficient method of *mstrn8*, however, did not yield a good approximation. Therefore, in *mstrnX*, the line and continuum absorption are unified and a new log-linear interpolation for pressure (26 grids) and a quadratic polynomial scaling for temperature (three grids) as shown below

$$k = k_0 \left(\frac{T}{T_0}\right)^{a+bT} \quad (3)$$

where k_0 is the absorption coefficient at a reference temperature T_0 (260 K) and fitting parameters, a and b, are the functions of absorption coefficients [20,21]. The absorption coefficient in each pressure and temperature are calculated by LBLRTM with HITRAN 2004. *Mstrn8* considers 16 species of halocarbons and heavy molecules in developing the weighted-averaged data [22] in each spectral band, while *MstrnX* considers 28 species complied in HITRAN 2004 and averaged in each spectral band.

2.3. Numerical integration in the CKD approach

2.3.1. Application to the optimization method

For numerical integrations in the k-distribution method, trapezoidal or Gaussian integration has been generally adopted in past studies [7]. It is known that an optimal integration scheme depends on the spectral interval under study because the accumulated probability density function (k-distribution) is a function of the absorption coefficient with a sharp peak near unity. For example, RRTM use 16 integration points in each band with three points necessary in the region where the k-distribution exceeds 0.99. Furthermore, the overlapping band problem increases the number of integration points.

Mstrn8 adopts a nonlinear optimization method, i.e., the sequential quadratic programming (SQP) method [23] to decrease the number of integration points, get better integration points and weights and optimize the overlapping problem at the same time. The transmission of the CKD method can be expressed integration over the cumulative probability and evaluated by a finite sum of exponential terms as below.

$$T = \int_0^1 \exp\{-k(g)m\}\,\mathrm{d}g = \sum_{i=1}^{n} \exp\{-k(x_i)m\}\Delta g_i \tag{4}$$

Here g is the cumulative probability, k is a function of an absorption coefficient in g-space, m is optical path, x_i and Δg_i is an ith quadrature point and weight, respectively, and n is the number of integration points. For spectral bands in which multiple gas absorption bands are considered, the transmission can be written as below

$$T = \sum_{i=1}^{n} \exp\left[-\left\{\sum_{j=1}^{n_{\mathrm{mol}}} k_j(x_{ij})m_j\right\}\right]\Delta g_i \tag{5}$$

where x_{ij} is an ith quadrature point of numerical integration for the jth gas and n_{mol} is the number of absorption gases in a spectral band. This method is an extended quasi-Newton method and we use to determine quadrature points $\{x_{ij}\}$ and weights $\{\Delta g_i\}$ for a numerical integration under an equality constraint.

$$\sum_{i=1}^{n} \Delta g_i = 1. \tag{6}$$

The inequality constraints are as follows:

$$\begin{cases} 0 \leqslant x_{ij} \leqslant 1 \\ \Delta g_i \geqslant 0 \end{cases} \quad (i = 1,\ldots,n; \quad j = 1,\ldots,n_{\mathrm{mol}}). \tag{7}$$

From these equations, the optimization problem has one equality and $(2n_{\mathrm{mol}}+1)n$ inequality constraints and has to be solved using a different n-value in each spectral band. With these constraints, the k-distribution parameters x_{ij} and Δg_i, are searched and determined so as to minimize the value of objective function.

The initial conditions of the quadrature for the SQP method are set as the squared of the Gaussian quadrature of the nth order

$$\begin{cases} x_{ij} = [t_i^2]_j \\ \Delta g_i = 2w_i t_i \end{cases} \tag{8}$$

where t_i and w_i are the points and weights, respectively, over the interval [0,1] of an n-point Gaussian quadrature rule, $\int_0^1 f(x)\,\mathrm{d}x = \sum_{i=1}^{n} w_i f(t_i)$. These t_i and w_i are calculated using Legendre polynomials. In *mstrn8*, for spectral bands in which multiple gas absorption bands are considered, a perfect correlated case is adopted for the initial condition. In this case, the transmission of n_{mol} gases is expressed as

$$T = \sum_{i=1}^{n} \Delta g_i \exp\left[-\left(\sum_{j=1}^{n_{\mathrm{mol}}} k_j(x_{ij})u_j\right)\right] \tag{9}$$

where u_j is the amount of the jth absorption gas and $k_j(x_{ij})$ are the absorption coefficients of the jth gas at the initial quadrature point x_{ij}.

We reconsider the initial condition and optimization process to get better solutions in *mstrnX*. One of the problems of the SQP method is known as the "local minima problem". In principle, the SQP method converges to the unique solution for any initial conditions and perturbations, however, the objective function sometimes becomes trapped at a local minimum without converging to the minimum of the entire search domain. We try to escape from this local minimum problem by introducing another initial condition and minimization process for *mstrnX*. Solutions obtained from different initial conditions usually trace different routes to convergence from which we then remove solutions, which have fallen into local minima. For this purpose, we attempt to test the following technique. First, we set the initial condition to a perfectly uncorrelated case in which the transmission of n_{mol} gases is expressed as follows:

$$T = \sum_{i_1=1}^{n}\sum_{i_2=1}^{n}\cdots\sum_{i_{n_{\mathrm{mol}}}=1}^{n}\Delta g_{i_1}\Delta g_{i_2}\cdots\Delta g_{i_{n_{\mathrm{mol}}}}\exp\left[-\left(\sum_{j=1}^{n_{\mathrm{mol}}}k_j(x_{ij})u_j\right)\right] \tag{10}$$

The number of integration points is $m = n^{n_{\mathrm{mol}}}$. Here, n is the prescribed order of the Gaussian quadrature used and n_{mol} is the number of gases considered in the spectral band. When the optimization process using this initial condition has converged, the point with the smallest effect on the objective function for this band is removed from the solution of the mth order; therefore, we use this removed condition as the initial condition for the $(m-1)$st order. The operation is repeated for all orders. In this study, this method is called the "decreasing method."

Fig. 3 shows an example of the difference between the original and decreasing method in the objective functions with a number of integration points in the 980–1175 cm^{-1} band. Except for one integration point case, the converged results are different and the objective function using the decreasing method is smaller than when using original method in the three, four and eight integration point cases. So the different initial condition is effective in some cases and we can select better solutions from converged results. Generally, the objective functions of both methods should monotonically decrease with an increase in the number of integration points, however, in this example it has not. It is supposed that a local minimum has been selected, the number of variables (i.e., the number of integration points and weights, mn_{mol}) prevent to converge and/or the number of iteration is not enough (this case is 50). This example indicates that some approaches are needed to find suitable solutions when the domain to search for the minimum objective function of several integration points includes multiple absorption bands.

2.3.2. Modification of the objective function

The objective function is defined in Eq. (1) as the sum of the errors in radiation fluxes and heating rate in *mstrn8*. We have modified this function for *mstrnX* to get the result within a chosen margin of error in each band. These criteria are described later. Moreover, this modification is needed because the optimized atmospheric altitude is varied up to 50 km (1 hPa) in the standard version of *mstrnX*, from 30 km (10 hPa) in the standard version of *mstrn8*, because an atmospheric altitude of 30 km (10 hPa) was found unsuitable for some applications of AGCM.

Firstly, we have new treatment for the weighting function for the heating rate error in the objective function. Because the heating rate is greater in the upper stratosphere than in the lower stratosphere and the troposphere when an absolute

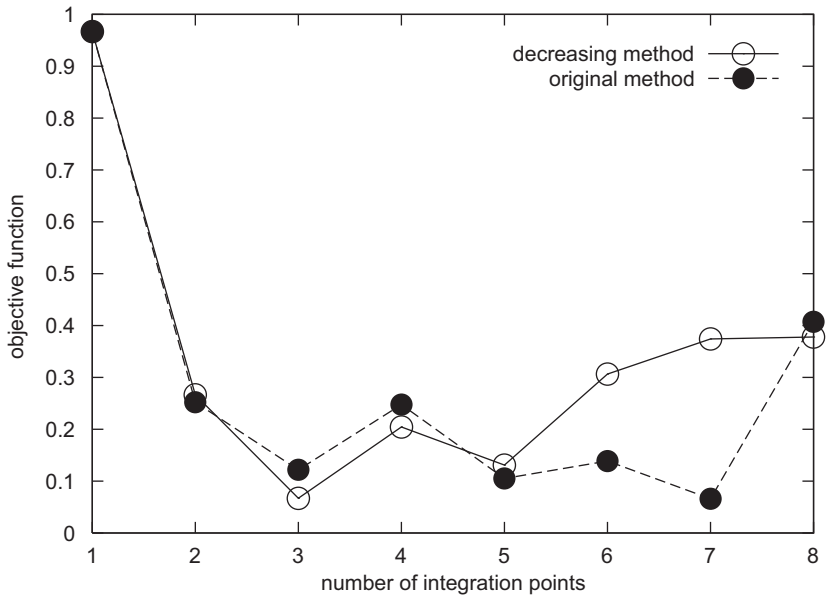

Fig. 3. Values of the objective function versus the number of integration points in the 980–1175 cm^{-1} band. Open circles with solid lines and filled circles with broken lines indicate the decreasing and original method, respectively.

error in each altitude is the same as that in the objective function, the relative error becomes large around the tropopause. We, therefore, have modified the contribution of the heating rate error in Eq. (1) as follows:

$$H_{\mathrm{err}} = \sum_{l=1}^{\mathrm{NL}} w(l)(h(l) - h_{\mathrm{lbl}}(l))^2 \Big/ \sum_{l=1}^{\mathrm{NL}} h_{\mathrm{lbl}}(l)^2, \quad \left(\sum_{l=1}^{\mathrm{NL}} w(l) = 1\right) \tag{11}$$

where $w(l)$ is the prescribed weighting function of the altitude. This weighting function is set large in the troposphere and small in the upper atmosphere.

A comparison of the heating rate profiles obtained using those weighting functions, which is calculated by three integration points in the 530–610 cm^{-1} band, is shown in Fig. 4. In this example, we assume the following three types of weighting functions:

$$\begin{aligned} w(l) &= 1 \text{ for } z(l) < 30\,\mathrm{km},\ 1/2 \text{ for } 30\,\mathrm{km} < z(l) < 50\,\mathrm{km} \text{ (type 1)} \\ &= 1 \text{ for } z(l) < 30\,\mathrm{km},\ 1/2 \text{ for } 30\,\mathrm{km} < z(l) < 70\,\mathrm{km} \text{ (type 2)} \\ &= 1 \text{ for } z(l) < 70\,\mathrm{km} \text{ (type 3)} \end{aligned} \tag{12}$$

Using type 1, the parameters are optimized to decrease errors in the heating rate for less than 50 km, so the error of the heating rate using type 1 is minimized up to 50 km and get the best results around 30 km. However, above 50 km, the error is larger than the others. Using type 3, we obtain a better result than using type 2 above 30 km. In the troposphere, all types give good results. We can control the error of heating rate to some extent using this weighting function.

Secondly, a weighting factor of radiation flux and heating rate errors is newly included. These two errors are not comparable and the ratio between flux and heating rate errors is different in each band. Sometimes one error is not fully decreased compared with the other when both errors are optimized using Eq. (1). Then, Eq. (1) is modified as below

$$f_{\mathrm{eval}} = \sqrt{\sum_{i\mathrm{atm}=1}^{6} (F_{\mathrm{err}}^2 + w_{\mathrm{ratio}} H_{\mathrm{err}}^2) \Big/ 6} \tag{13}$$

where w_{ratio} is the prescribed weighting factor of radiation flux and heating rate errors. Fig. 5 shows radiation flux and heating rate errors using two weighting factor ($w_{\mathrm{ratio}} = 1.0$ and 0.1) in the 530–610 cm^{-1} band. Compared the $w_{\mathrm{ratio}} = 0.1$ case (filled circles) with $w_{\mathrm{ratio}} = 1.0$ (open circles), the flux error is dramatically decreased but the heating rate error is slightly increased. We find the case of $w_{\mathrm{ratio}} = 0.1$ is suitable for this band. Thus, we apply the modifications described above and optimize the integration points and weights in several ways.

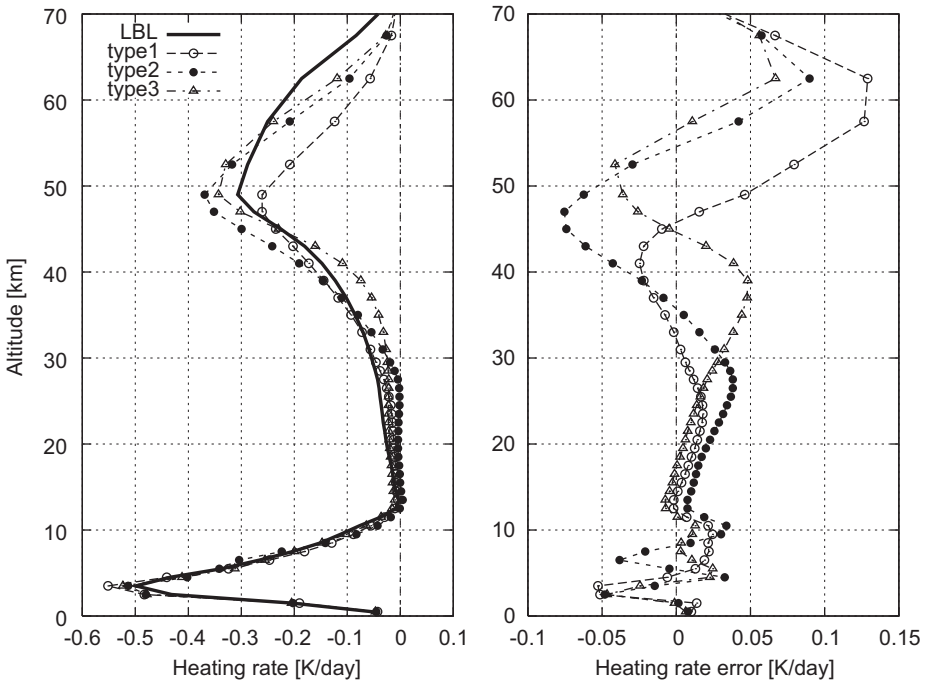

Fig. 4. The left figure shows the heating rate profiles in the 530–610 cm^{-1} band. Solid line indicates the LBL results, and types 1–3 indicate the prescribed weighting functions of the altitude. The right figure shows the difference in the profiles from the LBL results.

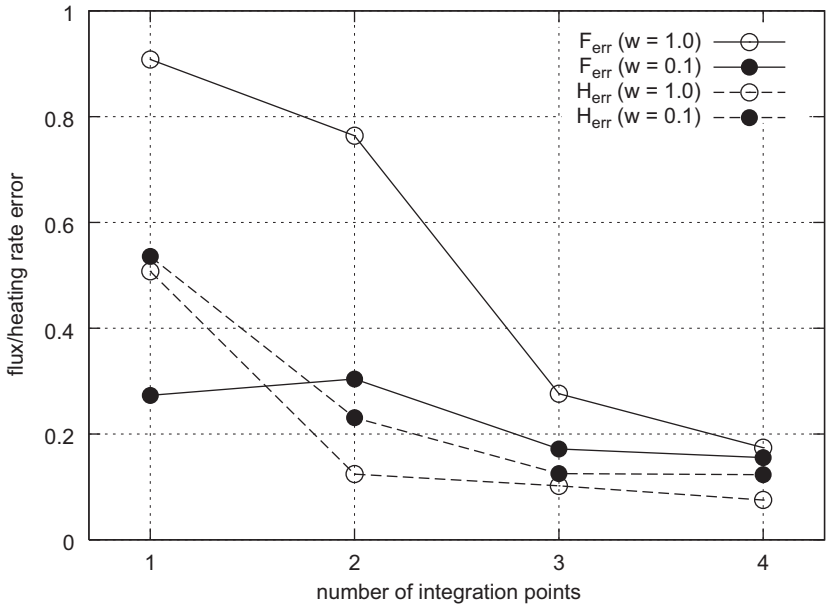

Fig. 5. Error norms of the radiation flux and heating rate versus the number of integration points in the 530–610 cm^{-1} band. Solid and broken lines indicate the ratio $w = 1.0$ and 0.1, open and filled circles indicate error norms of radiative flux and heating rate, respectively.

2.3.3. Determination for the number of integration points

The total number of integration points depends on the top of the model atmosphere and a predetermined level of accuracy. For example, in the standard version of *mstrnX*, we determined the margins of error for the radiation flux and heating rates to be 1.0 W/m^2 and 0.1 K/day in the LW and SW region, respectively, and select the result with the least number of integration points within those thresholds among the results obtained by several prescribed approaches in each band. From this, we determined a standard version with 18 bands and 40 integration points, which can be applied up to 50 km. For application to global warming experiments, we add another six atmospheric profiles in which the CO_2 concentration is doubled to optimize the *k*-distribution parameters in each band, which can then be applicable up to 70 km. Furthermore, we add another six profiles to the H_2O profile multiplied by 1.2 and/or CH_4 concentrations predicted for the years 2100 by IPCC [1] in the case of band accuracies are larger than the threshold below. It has accuracies to better than 0.5 W/m^2 for the net flux and 0.05 K/day for the heating rate error near the tropopause and lower stratosphere and 1.0 W/m^2 and 0.1 K/day in the upper stratosphere and mesosphere in each band of the LW and SW region. Moreover, when points and weights are determined in each band, we select the results whose errors in the instantaneous radiative forcing at TOA, troposphere and surface are under 0.2 W/m^2. A global warming version with 29 bands and 111 integration points has thus been developed. We also developed a "chemical version" with 37 bands and 126 integration points for chemical transport modeling. The band boundaries for bands longer than near-infrared spectral region are the same as those in the global warming version; however, the UV–vis spectral region is divided into greater number of bands and more integration points than in the other versions for a better computation of photo-dissociation reactions. Table 3 lists the spectral band allocation, implemented gas species and the number of integration points for the three versions.

3. Evaluation of *mstrnX*

Using the six AFGL standard atmospheres, we evaluate the accuracy of *mstrnX*. Table 4 shows the error norms of net flux at the TOA in the LW, at surface in the SW and that of the vertical-averaged (from surface up to 30, 50, and 70 km) heating rate averaged for the six AFGL standard atmospheres. *Mstrn8* is optimized up to 30 km, however, all values of *mstrnX* are significantly better than those of *mstrn8*. Similarly, in the standard version of *mstrnX*, the error norm of heating rate up to 70 km gets worse than up to 50 km. The tendency can be seen in the error profiles of the heating rate in Fig. 6. The error in the troposphere is significantly decreased from *mstrn8*. In the global warming version, the maximum radiation flux error is less than 0.6 W/m^2 in the LW and 0.45 W/m^2 in the SW at all altitudes (not shown), and the maximum heating rate error is less than 0.2 K/day in the troposphere and the stratosphere for any atmosphere.

In order to investigate the error partitioning of the improvements adopted in *mstrnX*, Fig. 7 shows the error profiles of the heating rate of (1) the *mstrn8* result —indicating the total error in *mstrn8*, (2) the LBL result using the absorption bands of all the major seven gases in HITRAN 92 with LOWTRAN 7—indicating updates of the databases, and (3) the LBL result using the absorption bands adopted by *mstrn8* in HITRAN 2004 with MT_CKD_1—indicating the influence of the number of

Table 4
Error norms of net flux at the TOA in the LW, net flux at the surface in the SW and vertical-averaged (up to 30, 50, and 70 km) heating rate averaged for the six AFGL standard atmospheres calculated by the global warming ("gw") and standard ("std") version of *mstrnX* and *mstrn8*

	LW			SW		
	gw	std	*mstrn8*	gw	std	*mstrn8*
Flux error	0.141	0.611	10.42	0.126	0.535	11.17
Heating rate error						
upto 30 km	0.061	0.161	0.298	0.034	0.066	0.261
upto 50 km	0.068	0.210	3.809	0.046	0.079	1.379
upto 70 km	0.088	1.096	4.619	0.059	0.170	1.929

Units are in W/m^2 and K/day.

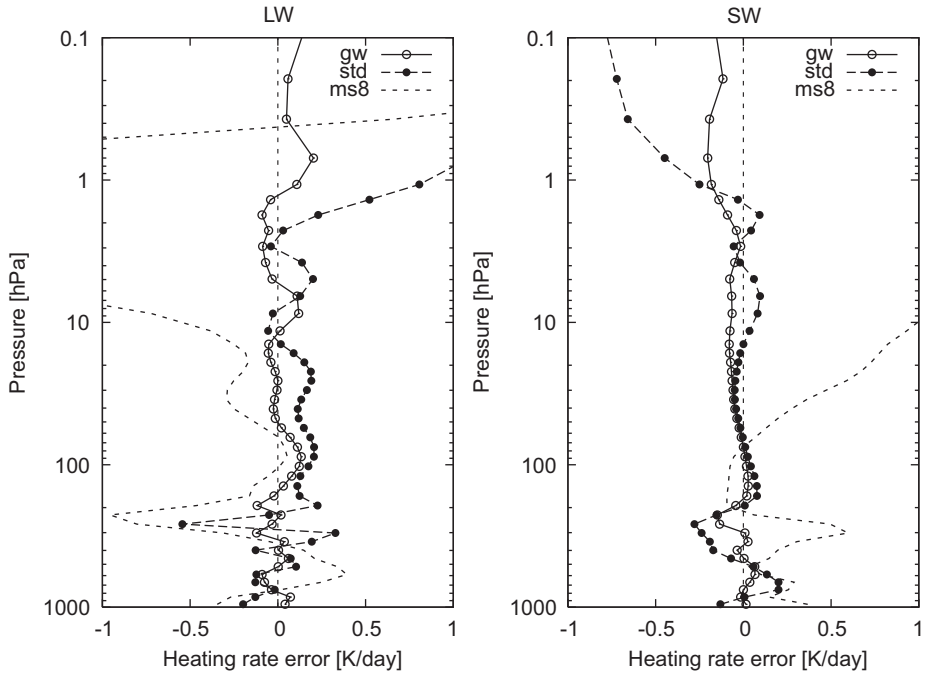

Fig. 6. Error profiles of the heating rate for the mid-latitude summer atmosphere calculated using *mstrnX*. The left and right figures are for the LW and SW regions, respectively. The open circles with solid line, filled circles with broken line and dotted line indicate the global warming version of *mstrnX*, the standard version of *mstrnX* and *mstrn8*, respectively.

absorption bands. In the LW region, the errors of *mstrn8* alone are much larger than those of the adopted database at all heights. For example, around the tropopause, the effect of band selection accounts for one third of the total error. In the SW region, the lack of several absorption bands in *mstrn8* is the largest source of error in the troposphere, however, the resulting effects are inconsequential in the stratosphere. This comparison suggests that the improvement in the accuracy of *mstrnX* is mainly attributed to the upgrade in the optimization scheme.

We should check the accuracy of *mstrnX* using atmospheric profiles that have not been used in the present optimization. For this purpose, we use domain- and time-averaged ECMWF Re-Analysis data, which has 23-layer from the surface to 1 hPa (about 50 km), dividing the globe into five regions—tropical (30S°–30N°), mid- (30°–60°) and high-latitude regions (60°–90°) in the northern and southern hemispheres. The data are averaged annually for the tropical and monthly (January and July) in the mid- and high-latitude regions. Using the above nine and two additional profiles—one with a convective condition and one with an inversion in the planetary boundary layer—we calculate the errors of both the radiation flux and the heating rate by using *mstrnX* and *mstrn8* as shown in Table 5. As compared with the results using the AFGL standard atmosphere (Table 4), the column-averaged errors of the radiation flux and the heating rate are larger. Based on this, a set of more realistic and greater number of atmospheric profiles should be used in the future for a better optimization.

In order to study the effects of global warming, an accurate radiation scheme, which can calculate instantaneous radiative forcing is needed. In the case of CO_2 doubling, errors in radiative forcing calculated using the standard version of

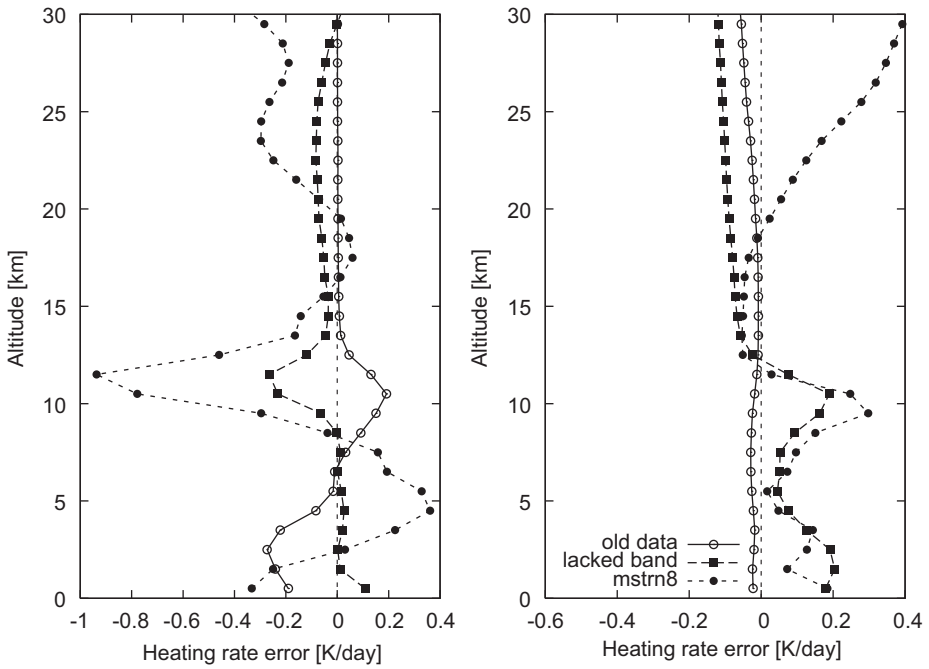

Fig. 7. The heating rate error profiles. LBL result using HITRAN 92 and LOWTRAN 7 (“old data”, broken lines with filled squares), LBL result adopting absorption bands treated in *mstrn8* (“lacked band”, solid lines with open circles), and *mstrn8* result (dotted lines with filled circles). Left and right panels represent the LW and SW regions, respectively.

Table 5
Same as in Table 4 but eleven averaged atmospheres from ECMWF Re-Analysis datasets have been used. Units are in W/m^2 and K/day

	LW			SW		
	gw	std	*mstrn8*	gw	std	*mstrn8*
Flux error	0.236	1.104	10.69	0.123	0.302	5.957
Heating rate error	0.119	0.671	1.438	0.042	0.113	1.825

mstrnX and *mstrn8* are much larger than those calculated using the global warming version of *mstrnX*. This result indicates that the optimization using only six standard AFGL atmosphere could not deal with a doubling CO_2 condition. As commonly acknowledged, these weak absorption bands should be treated carefully in global warming experiments. We find that an increase in the number of integration points in the weak CO_2 absorption bands is not an effective solution because the heating rate profiles in the doubling condition differ considerably from those in AFGL standard atmospheres leading to an increase in error in the stratosphere. This is the reason why the different profiles in gas concentrations are introduced for the global warming version.

Here, we consider eight RTMIP test cases and compare the radiative forcing of increasing greenhouse gases. Tables 6 and 7 show radiative forcing in seven cases at the TOM (top of model), 200 hPa (around the tropopause) and the surface. The experimental configuration used is that of RTMIP. The result of *mstrnX* is from the global warming version. $\langle F_{\mathrm{gcm}} \rangle$ and $\langle F_{\mathrm{lbl}} \rangle$ are the mean of the samples of forcings from the AGCMs and LBL models, which are participating in RTMIP. Most results of *mstrnX* are feasible and within one standard deviation of the samples of forcings from the AGCMs. Compared with the forcings in the LBL models, the difference in *mstrnX* are smaller than those of the AGCMs models at any level for changes in CO_2 concentration from 1860 to 2000 values (case 2a-1a) and from 1860 to double 1860 values (case 2b-1a). In some forcing cases, the AGCMs cannot be evaluated the effect of CO_2 in the SW, however, *mstrnX* can. In the forcing case for changes in N_2O and CFCs from 1860 to 2000 values (case 3b-3c), the results of *mstrnX* in the LW are not good. It is thought that one of the reasons for this is that our LBL result in this case is smaller than the mean forcing of AGCM and LBL models, suggesting our experimental set up for this case is not the same as in the LBL simulation of RTMIP. Further investigation is needed on this point.

Lastly, we study the impact of the updated radiation schemes on the CCSR/NIES AGCM simulations. We carry out the CCSR/NIES AGCM simulations using the standard version of *mstrnX* with a horizontal resolution of *T42* and a vertical

Table 6
Longwave results for the seven forcing cases

Level	Field	Forcing cases						
		2a-1a	2b-1a	3b-3a	3a-1a	3b-3c	3b-3d	4a-2b
TOM	*MstrnX*	1.03	2.92	2.13	3.87	0.13	0.95	3.47
TOM	$\langle F_{\mathrm{gcm}} \rangle$	0.08	2.45	2.19	3.61	0.59	1.10	3.57
TOM	$\langle F_{\mathrm{lbl}} \rangle$	1.01	2.80	2.09	3.63	0.48	0.93	3.78
200 hPa	*MstrnX*	2.02	5.73	3.13	3.47	0.13	0.95	4.33
200 hPa	$\langle F_{\mathrm{gcm}} \rangle$	1.82	5.07	2.95	3.37	0.47	0.95	4.45
200 hPa	$\langle F_{\mathrm{lbl}} \rangle$	1.95	5.48	3.00	3.47	0.41	0.89	4.57
Surface	*MstrnX*	0.50	1.61	0.61	0.54	0.01	0.08	12.25
Surface	$\langle F_{\mathrm{gcm}} \rangle$	0.38	1.12	1.21	1.80	0.43	0.74	11.95
Surface	$\langle F_{\mathrm{lbl}} \rangle$	0.57	1.64	1.08	1.14	0.28	0.46	11.52

Cases 2a-1a and 2b-1a are forcings for changes in CO_2 concentrations from 1860 to 2000 values and from 1860 to double 1860 value, respectively, case 3b-3a is a forcing for changes in WMGHGs from 1860 to 2000 values, case 3a-1a is in CH_4 and N_2O from zero to 1860 values, case 3b-3c is in N_2O and CFCs from 1860 to 2000 values, case 3b-3d is in CH_4 and CFCs from 1860 to 2000 calues, and case 4a-2b is increased H_2O predicted when CO_2 is doubled. "*MstrnX*" indicates the global warming version of *mstrnX*. $\langle F_{\mathrm{gcm}} \rangle$ and $\langle F_{\mathrm{lbl}} \rangle$ are the mean of the samples of forcings from the AOGCMs and LBL models in the Table 8 of Collins et al. [7]. Units are in W/m^2.

Table 7
Same in Table 6 but in the shortwave

Level	Field	Forcing cases						
		2a-1a	2b-1a	3b-3a	3a-1a	3b-3c	3b-3d	4a-2b
TOM	*MstrnX*	0.03	0.07	0.07	0.04	0.00	0.04	0.78
	$\langle F_{\mathrm{gcm}} \rangle$	0.07	0.21	0.07	0.00	0.00	0.00	0.63
	$\langle F_{\mathrm{lbl}} \rangle$	0.04	0.12	0.13	0.15	0.00	0.09	0.75
200 hPa	*MstrnX*	−0.26	−0.76	−0.69	−0.38	0.00	−0.43	0.70
	$\langle F_{\mathrm{gcm}} \rangle$	−0.27	−0.79	−0.27	0.00	0.00	0.00	0.37
	$\langle F_{\mathrm{lbl}} \rangle$	−0.27	−0.77	−0.41	−0.35	−0.02	−0.13	0.51
Surface	*MstrnX*	−0.21	−0.63	−0.45	−0.22	0.00	−0.24	−6.02
	$\langle F_{\mathrm{gcm}} \rangle$	−0.49	−1.47	−0.49	0.00	0.00	0.00	−4.89
	$\langle F_{\mathrm{lbl}} \rangle$	−0.32	−0.96	−0.86	−0.95	−0.02	−0.53	−5.87

Values of $\langle F_{\mathrm{gcm}} \rangle$ and $\langle F_{\mathrm{lbl}} \rangle$ are in the Table 9 of Collins et al [7]. Units are in W/m^2.

resolution of *L20* to analyze the temperature field in the last 5 years of 10-year runs as shown in Fig. 8. This simulation with *mstrnX* is identical to the one using *mstrn8* as shown in Fig. 2. Figs. 2 and 8 show that the cold bias around the tropopause decreases considerably with this improvement in the radiation code. However, the cold bias persists around the high latitude in the winter hemisphere and a warm bias appears at the tropopause at the winter pole. Such phenomena are considered to be counter effects of physical parameter tuning in the AGCM originally designed to offset the bias introduced by using *mstrn8*.

4. Conclusions

In this paper, we have updated the gas absorption scheme in the radiative transfer code "*mstrn8*" to "*mstrnX*." The improvements are as follows:

- Adoption of the latest gas absorption parameter database "HITRAN 2004" and continuum absorption model "MT_CKD_1".
- Introduction of a new selection rule for gas absorption bands and increase in the number of absorption bands.
- Improvement in the initial conditions and selection methods of the quadrature points and weights used for the CKD and adoption of a weighting function for the altitude and ratio of flux and heating rate error used for the objective function in the optimization method.

These changes have significantly improved the simulation of the radiation budget.

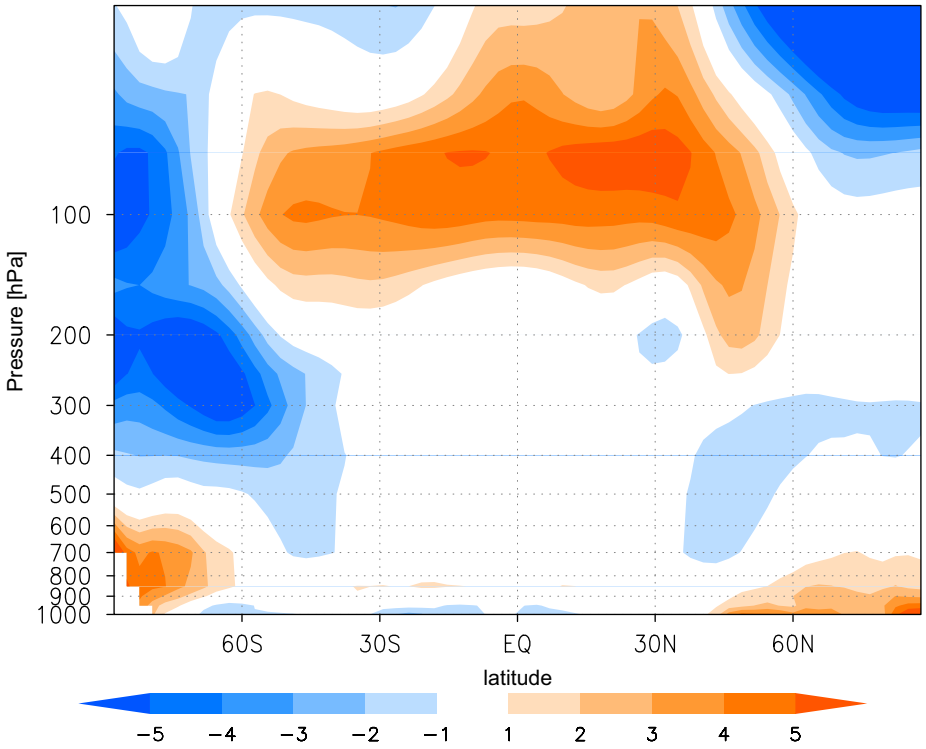

Fig. 8. Same as in Fig. 2 but using *mstrnX*.

Concerning the updating of the gas absorption parameter, the maximum difference in LW heating rate between the old and new databases is about 0.3 K/day in the lower troposphere, however, it has a minor effect as compared with the other improvements. The new selection rule for gas absorption bands uses a score function for determining the importance of gas absorption bands in the total absorption. By adopting this selection rule, the number of absorption bands included in *mstrnX* is greater than those in *mstrn8*. A test calculation with gas absorption bands considered in *mstrn8* for LBL calculation has yielded a flux error of about 3–5 W/m^2, whereas of the flux error of *mstrnX* does not exceed 0.1 W/m^2.

The contributing improvement the most is the change in the optimization process for selecting the quadratures used for the numerical integration. We add a different approach to search for better solutions for integration points and weights and the altitude for which the radiation code has small errors from 30 to 50 or 70 km. Moreover, a weighting function for the altitude and the ratio of radiation flux and heating rate error is introduced to the objective function to make it small and those feasible values in each band are different. In this condition, the new optimization algorithm produced 18 bands and 40 integration points for the standard version with a top height of 50 km. In this version, the maximum heating rate errors below 30 km are within 0.2 K/day except around tropopause for any atmosphere. This version is not suitable for a long-term GCM simulation or a calculation of radiative forcing, however, suitable for the models which require many calculations in short-term simulations, like a cloud-resolving model, and has achieved good results [24].

For global warming conditions, we add other atmospheres which are increased in gas concentrations to the optimized profiles and, along with a radiative forcing constraint, selected a new number of integration points in each band. From this, we subsequently build a global warming version with 29 bands and 111 integration points with a top height of 70 km. In this version, the maximum radiation flux error is less than 0.6 W/m^2 in the LW and 0.45 W/m^2 in the SW at all altitude, and the maximum heating rate error is less than 0.2 K/day in the troposphere and the stratosphere for any atmosphere. Using these ideas, radiative forcings can be evaluated which contain errors not exceeding one standard deviation of the samples of forcings from the AGCMs used in the RTMIP experiment except for the changes of N_2O+CFCs case. This version is suitable for a long-term calculation and is adopted to CCSR/NIES AGCM, which is participated in the IPCC fourth assessment report. A numerical integration of the CCSR/NIES AGCM with *mstrnX* suppressed the known cold bias in the lower stratosphere, which frequently appeared in simulations using *mstrn8*.

It is found that the proposed optimization method is effective in maintaining a low computational cost with accuracy good enough for dynamical simulations with a GCM. We plan to overcome some remaining issues and make accurate versions that require a greater number of bands and integration points, a number of atmospheric conditions and gas concentrations for improving the accuracy of future simulations for various applications. *MstrnX* is specialized for the solar and terrestrial radiation, but this study can be applied to another planet and a Mars version is under development. *MstrnX* is now available from the OpenCLASTR project website (http://www.ccsr.u-tokyo.ac.jp/~clastr).

Acknowledgments

This research was supported by the Global Environment Research Fund by the Ministry of Environment Japan B-4 and by RR2002 project of Ministry of Science, Sports, and Culture.

References

[1] Houghton JT, Ding Y, Griggs DJ, Noguer M, van Linden PJ, Xiaosu D, editors. Intergovernmental Panel on Climate Change (IPCC), climate change 2001: the scientific basis. USA: Cambridge University Press; 2001.
[2] Ellingson RG, Ellis J, Fels S. The intercomparison of radiation codes used in climate models: long wave results. J Geophys Res 1991;96:8929–53.
[3] Fouquart Y, Bonnel B, Ramaswamy V. Intercomparing shortwave radiation codes for climate studies. J Geophys Res 1991;96:8955–68.
[4] Collins WD, et al. Radiative forcing by well-mixed greenhouse gases: estimates from climate models in the Intergovernmental Panel on Climate Change (IPCC) Fourth Assessment Report (AR4). J Geophys Res 2006;111:14317–31.
[5] Lacis AA, Oinas V. A description if the correlated *k* distribution method for modeling nongray gaseous absorption, thermal emission, and multiple scattering in vertically inhomogeneous atmospheres. J Geophys Res 1991;96:9027–63.
[6] Fu Q, Liou KN. On the correlated *k*-distribution method for radiative transfer in nonhomogeneous atmospheres. J Atmos Sci 1992;49:2139–56.
[7] Mlawer EJ, Taubman SJ, Brown PD, Iacono MJ, Clough SA. Radiative transfer for inhomogenerous atmospheres: RRTM, a validated correlated-*k* model for longwave. J Geophys Res 1997;102:16663–82.
[8] Morcrette JJ. Radiation and cloud radiative properties in the European Center for Medium Range Weather Forecasts Forecasting System. J Geophys Res 1991;96:9121–32.
[9] Iacono MJ, Mlawer EJ, Clough SA, Morcrette JJ. Impact of an improved longwave radiation model, RRTM, on the energy budget and thermodynamic properties of the NCAR community climate model, CCM3. J Geophys Res 2000;105:14873–90.
[10] Chevallier F, Morcrette JJ, Chéruy F, Scott NA. Use of a neural-network based long-wave radiative-transfer scheme in the ECMWF atmospheric model. Q J R Meteorol Soc 2000;126:761–76.
[11] Kiehl JT, Hack JJ, Bonan GB, Boville BA, Briegleb BP, Williamson DL, et al. Description of the NCAR community climate model (CCM3). NCAR Technical note, NCAR/TN-420+STR, National Center for Atmospheric Research, Boulder, CO, 1996.
[12] Kiehl JT, Hack JJ, Bonan GB, Boville BA, Williamson DL, Rasch PJ. The national center for atmospheric research community climate model: CCM3. J Clim 1998;11:1131–49.
[13] Nakajima T, Tsukamoto M, Tsushima Y, Numaguti A, Kimura T. Modeling of the radiative process in an atmospheric general circulation model. Appl Opt 2000;39:4869–78.
[14] Nakajima T, Tanaka M. Matrix formulations for the transfer of solar radiation in a plane-parallel scattering atmosphere. JQSRT 1986;35:13–21.
[15] Rothman LS, et al. The HITRAN 2004 molecular spectroscopic database. JQSRT 2005;96:139–204.
[16] Clough SA, Iacono MJ, Moncet JL. Line-by-line calculations of atmospheric fluxes and cooling rates: application to water vapor. J Geophys Res 1992;97:15761–85.
[17] Clough SA, Iacono MJ. Line-by-line calculation of atmospheric fluxes and cooling rates. 2. Application to carbon dioxide, ozone, methane, nitrous oxide and the halocarbons. J Geophys Res 1995;100:16519–35.
[18] Clough SA, Shephard MW, Mlawer EJ, Delamere JS, Iacono MJ, Cady-Pereira K, Boukabara S, Brown PD. Atmospheric radiative transfer modeling: a summary of the AER codes. JQSRT 2005;91:233–44.
[19] Liou KN. Radiation and cloud processes in the atmosphere. New York: Oxford University Press; 1992.
[20] Shi GY. On correlated k distribution model in radiative calculation. Chin J Atmos Sci 1998;22:659–76.
[21] Zhang H, Nakajima T, Suzuki T, Imasu R, Shi GY. An optimal approach to overlapping bands with correlated *k*-distribution and their application to radiative calculation in climate models. J Geophys Res 2003;108:4641–53.
[22] Shi GY. Radiative forcing and greenhouse effect due to atmospheric trace gases. Sci Sin Ser B 1992;35:217–29.
[23] Ibaraki T, Fukushima M. FORTRAN77 optimization programming. Tokyo: Iwanami-shoten; 1991. 480pp.
[24] Miura H, Satoh M, Nasuno T, Noda AT, Oouchi K. A Madden–Julian oscillation event realistically simulated by a global cloud-resolving model. Science 2007;318:1763–5.